Novel Generic Asymmetric and Symmetric Equivalent Circuits of 90° Coupled Transmission-Line Sections Applicable to Marchand Baluns

Hee-Ran Ahn, *Senior Member, IEEE,* and Manos M. Tentzeris, *Fellow, IEEE*

Abstract—Three different equivalent circuits (asymmetric, symmetric, and mixed) of the 90° coupled transmission-line sections are proposed for Marchand baluns, including the accurate modeling of the effect of the connecting segment. The asymmetric one consists of one set of coupled transmission-line sections and two identical uncoupled transmission-line sections. Due to the asymmetry and a four-port circuit configuration, it seems to be difficult to derive the design formulas for the asymmetric equivalent circuit, thus leading to their indirect derivation by adding two identical transmission-line sections with effectively "negative" electrical lengths to the original 90° coupled transmission-line sections. The symmetric one may be obtained by combining the even- and odd-mode equivalent circuits, while the mixed equivalent circuit is combining the asymmetric and the symmetric ones. As a proof-of-concept, a symmetric and an asymmetric equivalent circuits along with a Marchand balun with a connecting section were implemented at 2 GHz, demonstrating a very good agreement between the simulated and the experimental values.

Index Terms—Asymmetric, symmetric and mixed equivalent circuits of 90° coupled transmission-line sections, directional couplers, impedance transforming Marchand baluns, Marchand baluns with the connecting segments, power dividers.

I. INTRODUCTION

IN THE past, the balanced-to-unbalanced transformers (baluns) [1]–[11] have been extensively utilized for various applications, such as balanced mixers, balanced amplifiers, and frequency multipliers and have been implemented in different forms and configurations. One of them is the Marchand balun [1], consisting of two sets of coupled 90° transmission-line sections. If the two coupled transmission-line sections are identical, a 180° phase difference between the two balanced ports can be achieved theoretically in all frequencies except at even multiples of the design frequency (practically over very wide frequency bands) when no isolation circuit is connected.

Due to this attractive inherent feature, the Marchand baluns have received substantial attention from the microwave circuit designers.

However, since two coupled transmission-line sections are connected together, the two balanced ports of the Marchand baluns should be inherently connected together, which typically complicates the fabrication process. To solve this problem, a significant amount of research has been reported in the past [6]–[11]. A transmission-line section in [6] and an artificial transmission-line section in [7] are, however, connected between two coupled-line sections, but theoretical correctness does not seem to have been clarified. In [8], an approximate compensation for the connecting segment is applied by considering the two coupled-line sections different, but the overall frequency responses seem to be undesirable. In [9], exact design formulas have been derived to compensate for the connecting segments, but they are valid only for equal termination impedances and for a coupling coefficient of −4.77 dB of the Marchand baluns. In [10], even though the exact solution is available in [9], a more challenging generalized example [10] is demonstrated, because two different sets of asymmetric coupled transmission-line sections are implemented. In [11], the connecting segment was applied to the impedance-transforming Marchand baluns, although no near-perfect matching could be achieved, while the featured bandwidths and the phase differences between the two output ports deteriorated for longer connecting segments [11, Fig. 3], due to the lack of phase compensation loads, which will be discussed in the following.

To overcome these problems stemming from the previously reported conventional models, various novel generic asymmetric, symmetric, and mixed equivalent circuits of the 90° coupled transmission-line sections are introduced in this paper so that the connecting segment topologies can be applied to any Marchand balun regardless of the termination impedances and the coupling coefficients.

The proposed asymmetric equivalent circuit consists of one set of coupled transmission-line sections with arbitrary electrical lengths and two identical uncoupled transmission-line sections connected to two ports of the coupled-line topology in a diagonal fashion. However, due to the lack of symmetry in this circuit, it is quite complicated to derive the exact design formulas. To make the algebraic manipulation much simpler,
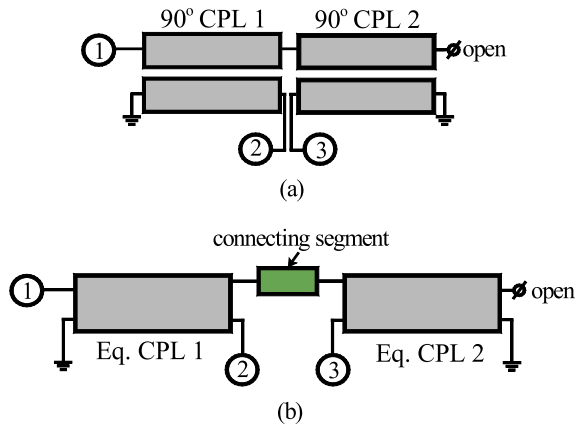
Fig. 1. Marchand baluns. (a) Marchand balun. (b) Marchand balun with a connecting segment.

two identical uncoupled transmission-line sections, which are of the same characteristic impedances but featuring effectively "negative" electrical lengths, are added to the 90° coupled transmission-line topology and its asymmetric equivalent circuit. As a result, the number of unknown variables can be reduced, by which the design of the asymmetric equivalent circuits may be feasible. The symmetric equivalent circuit is composed of one set of coupled transmission-line sections and four identical uncoupled transmission-line sections. The mixed equivalent circuit is similar to the symmetric one in the regard that a set of coupled transmission-line sections and four uncoupled transmission-line sections are necessary, but asymmetric due to the different lengths of the uncoupled transmission line sections. Therefore, the mixed one features asymmetric and symmetric properties at the same time. Any equivalent circuit may be applied to the Marchand baluns with the connecting segments, but the conventional designs [9] are limited to one of three cases produced by the asymmetric equivalent circuits, which will be clarified further with the impedance-transforming Marchand baluns [5].

To verify the suggested theory, symmetric, asymmetric equivalent circuit prototypes and a Marchand balun prototype were designed at $f_0 = 2$ GHz and were fabricated on a substrate (RT/duroid 5870, $\varepsilon_r = 2.33$, and $H = 31$ mil) with the microstrip technology. The symmetric and asymmetric ones model a 50 Ω and an impedance-transforming (35 into 50 Ω) directional couplers [12], respectively, with a coupling coefficient of -3 dB. The Marchand balun transforms 100 into 50 Ω.

II. EQUIVALENT CIRCUITS OF 90° COUPLED TRANSMISSION-LINE SECTIONS

A Marchand balun consists of two 90° coupled transmission-line sections with two ports closely connected together, as shown in Fig. 1(a). Due to the inherent structure of the Marchand balun, the realization of two balanced ports at ports ② and ③ may not be easy. To enable the fabrication of these two ports in a way allowing their easy interconnect to other circuits, any circuit additionally having uncoupled transmission-line sections, being equivalent to the 90° coupled transmission-line sections, is needed to
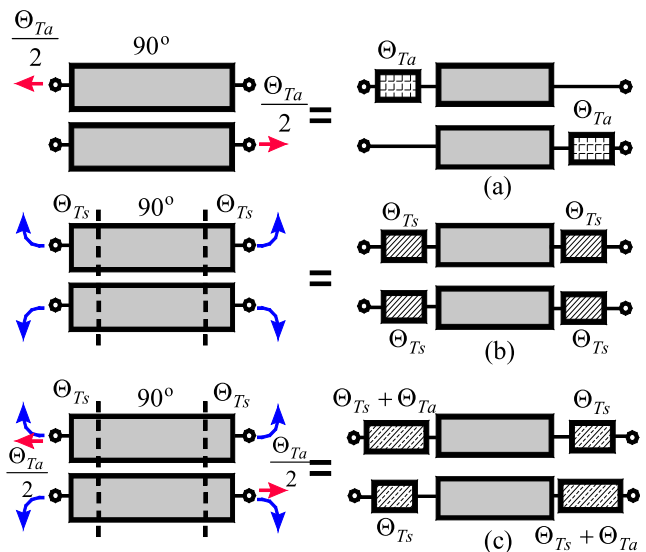

Fig. 2. Basic principle of the equivalent circuits. (a) Asymmetric equivalent circuit. (b) Symmetric equivalent circuit. (c) Mixed equivalent circuit.

keep the two coupled transmission-line sections apart from each other, as shown in Fig. 1(b). For this purpose, three different equivalent circuits (asymmetric, symmetric, and mixed) will be investigated.

The basic principle for the equivalent circuits is as follows. A set of 90° coupled transmission-line sections is shown in the left side in Fig. 2(a). To allow for the existence of uncoupled transmission-line sections featuring a similar performance, it could be possible to move the upper coupled transmission-line section to the left by $\Theta_a/2$ and the lower one to the right by $\Theta_a/2$ to maintain a center symmetry, which results in the asymmetric form in Fig. 2(a). Another way is to broaden the coupling gap at both sides to guarantee the lack of significant coupling at least within each edge length of Θ_{Ts}. The resulting configuration is symmetric, as shown in Fig. 2(b). The third way combines the above two approaches, leading to the equivalent circuit shown in Fig. 2(c), which is called a mixed equivalent circuit. All equivalent circuits in Fig. 2(a)–(c) are center symmetric and therefore can be equivalent to the 90° coupled transmission-line sections. The names of "asymmetric," "symmetric," and "mixed" are chosen to distinguish from each other.

A. Asymmetric Equivalent Circuits

The 90° coupled transmission-line topology and its asymmetric equivalent circuit are shown in Fig. 3(a) and (b), where Y_{0eR}, Y_{0oR}, and C_0 represent the even- and odd-mode admittances and the coupling coefficient of the 90° coupled transmission-line sections, respectively. The equivalent circuit in Fig. 3(b) consists of one pair of coupled transmission-line sections and two identical uncoupled transmission-line sections connected to two ports of the coupled transmission-line sections in a diagonal fashion. The even- and odd-mode admittances of the coupled transmission-line sections of the asymmetric equivalent circuit in Fig. 3(b) are Y_{0ea} and Y_{0oa}, and the electrical length of their coupled section is Θ_a. The characteristic impedance and the electrical length of each uncoupled transmission-line section are Z_T and Θ_{Ta},
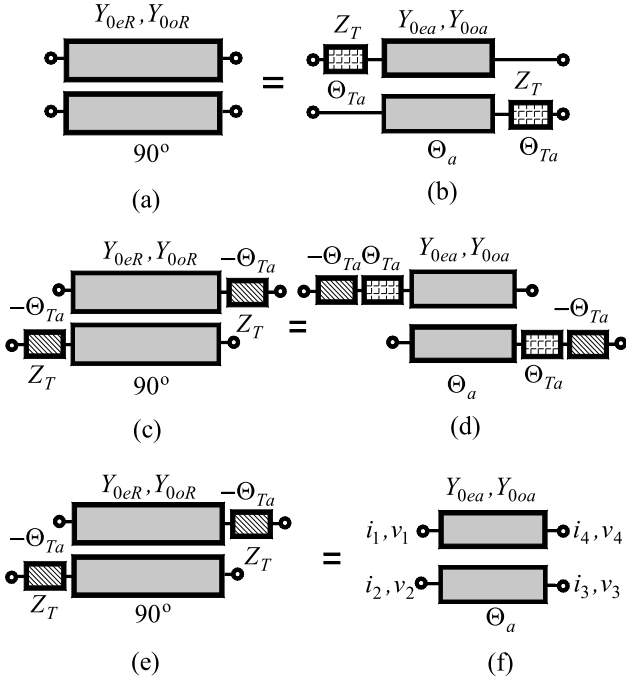
Fig. 3. Set of 90° coupled-line sections and its asymmetric equivalent circuit. (a) 90° coupled transmission-line sections. (b) Asymmetric equivalent circuit. (c) and (d) Adding transmission-line sections with negative length of $-\Theta_{Ta}$. (e) and (f) Resulting circuits.

where Z_T is

$$Z_T^{-1} = Y_T = \sqrt{Y_{0eR}Y_{0oR}}. \tag{1}$$

Due to the lack of symmetry in the asymmetric equivalent circuit in Fig. 3(b), it is not possible to apply even- and odd-mode excitation analysis, necessitating the need for a full four-port analysis. To make the calculation process simpler, adding two identical uncoupled transmission-line sections with Z_T of a negative electrical length of $-\Theta_{Ta}$ to both circuits in Fig. 3(a) and (b) leads to the circuits shown in Fig. 3(c) and (d). Since two cascaded transmission-line sections with Θ_{Ta} and $-\Theta_{Ta}$ in Fig. 3(d) are overall equivalent to no transmission-line section connected, the two transmission-line sections in Fig. 3(b) disappear, effectively leaving only the one set of coupled transmission-line sections shown in Fig. 3(f). That is, the relationship between the two topologies shown in Fig. 3(a) and (b) is identical to the one between those shown in Fig. 3(e) and (f). In Fig. 3(b), there are four admittance parameters including three unknown variables of Y_{0ea}, Y_{0oa}, and Θ_a of the coupled-line sections in Fig. 3(b) that are combined with two identical transmission-line sections, which leads to very complicated calculations for the design formulas. In the relation between the two in Fig. 3(e) and (f), however, since the 90° coupled-line sections have only two known (given) variables, Y_{0eR} and Y_{0oR}, the calculation becomes much simpler.

To derive the design formulas of Y_{0ea}, Y_{0oa}, and Θ_a, the circuit with the 90° coupled transmission-line sections in Fig. 3(e) is again shown in Fig. 4, where the different currents of i_1, i_2, i_{2m}, i_3, i_4, and i_{4m} and voltages of v_1, v_2, v_{2m}, v_3, v_4, and v_{4m} are indicated.
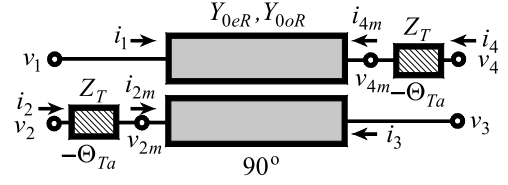

Fig. 4. Coupled-line topology equivalent to that in Fig. 3(f).

The admittance parameters of the 90° coupled transmission-line topology with Y_{0eR} and Y_{0oR} in Fig. 4 are

$$\begin{bmatrix} i_1 \\ i_{2m} \\ i_3 \\ i_{4m} \end{bmatrix} = \begin{bmatrix} 0 & 0 & A_{13} & A_{14} \\ 0 & 0 & A_{14} & A_{13} \\ A_{13} & A_{14} & 0 & 0 \\ A_{14} & A_{13} & 0 & 0 \end{bmatrix} \begin{bmatrix} v_1 \\ v_{2m} \\ v_3 \\ v_{4m} \end{bmatrix} \tag{2}$$

where i_1, i_{2m}, i_3, i_{4m}, v_1, v_{2m}, v_3, and v_{4m} are the corresponding currents and voltages, and A_{13} and A_{14} [13] are given by

$$A_{13} = j(Y_{0eR} - Y_{0oR})/2 \tag{2a}$$
$$A_{14} = j(Y_{0eR} + Y_{0oR})/2. \tag{2b}$$

As indicated in (2a) and (2b), the variables required for the calculation of the admittance matrix are only two and they are already known (given). The relations between the currents of $i_{2m,4m}$ and $i_{2,4}$ and the voltages of $v_{2m,4m}$ and $v_{2,4}$ in Fig. 4 are

$$\begin{bmatrix} -i_{2m,4m} \\ i_{2,4} \end{bmatrix} = \begin{bmatrix} T_{11} & T_{12} \\ T_{21} & T_{22} \end{bmatrix} \begin{bmatrix} v_{2m,4m} \\ v_{2,4} \end{bmatrix} \tag{3}$$

where $i_{2m,4m}$ is meant as i_{2m} or i_{4m}, $v_{2m,4m}$ as v_{2m} or v_{4m}, and T_{ij} are representing the admittance parameters of two identical transmission-line sections with $Y_T = Z_T^{-1}$ and negative length of $-\Theta_{Ta}$ in [14]

$$T_{11} = T_{22} = jY_T\cot\Theta_{Ta} \tag{3a}$$
$$T_{12} = T_{21} = -jY_T\csc\Theta_{Ta}. \tag{3b}$$

From (3), both of i_{2m} and i_{4m} and v_{2m} and v_{4m} can be expressed in terms of i_2 and i_4 and v_2 and v_4 such as

$$i_{2m} = T_{11}(T_{22}v_2 - i_2)T_{21}^{-1} - T_{12}v_2 \tag{4a}$$
$$v_{2m} = (i_2 - T_{22}v_2)T_{21}^{-1} \tag{4b}$$
$$i_{4m} = T_{11}(T_{22}v_4 - i_4)T_{21}^{-1} - T_{12}v_4 \tag{4c}$$
$$v_{4m} = (i_4 - T_{22}v_4)T_{21}^{-1}. \tag{4d}$$

Substituting the values of i_{2m}, v_{2m}, i_{4m}, and v_{4m} in (4) into (2) and applying the relation of $T_{11}T_{22} - T_{12}^2 = Y_T^2$ gives

$$\begin{bmatrix} T_{11} & A_{13} \\ A_{13} & T_{11} \end{bmatrix} \begin{bmatrix} i_2 \\ i_4 \end{bmatrix} = \begin{bmatrix} Y_T^2v_2 - A_{14}T_{21}v_3 + A_{13}T_{22}v_4 \\ -A_{14}T_{21}v_1 + A_{13}T_{22}v_2 + Y_T^2v_4 \end{bmatrix}. \tag{5}$$

Finally, the currents i_2 and i_4 in (5) can be expressed as

$$i_2 = \psi_1v_1 + \psi_2v_2 + \psi_3v_3 + \psi_4v_4 \tag{6a}$$
$$i_4 = \phi_1v_1 + \phi_2v_2 + \phi_3v_3 + \phi_4v_4 \tag{6b}$$

where

$$\psi_1 = \phi_3 = A_{13}A_{14}T_{21}D^{-1} \tag{6c}$$

$$\psi_2 = \phi_4 = T_{22}(Y_T^2 - A_{13}^2)D^{-1} \tag{6d}$$

$$\psi_3 = \phi_1 = -T_{11}T_{21}A_{14}D^{-1} \tag{6e}$$

$$\psi_4 = \phi_2 = T_{12}^2 A_{13}D^{-1} \tag{6f}$$

with

$$D = T_{11}^2 - A_{13}^2. \tag{6g}$$

The admittance parameters [13] of the coupled-line topology in Fig. 3(f) are

$$\begin{bmatrix} i_1 \\ i_2 \\ i_3 \\ i_4 \end{bmatrix} = \begin{bmatrix} B_{11} & B_{12} & B_{13} & B_{14} \\ B_{12} & B_{11} & B_{14} & B_{13} \\ B_{13} & B_{14} & B_{11} & B_{12} \\ B_{14} & B_{13} & B_{12} & B_{11} \end{bmatrix} \begin{bmatrix} v_1 \\ v_2 \\ v_3 \\ v_4 \end{bmatrix} \tag{7}$$

where if the even-mode electrical length of Θ_{ae} is assumed to be the same as the odd-mode one of Θ_{ao} without loss of generality as their difference is typically very small, or, $\Theta_{ea} = \Theta_{oa} = \Theta_a$, the values of B_{11}, B_{12}, B_{13}, and B_{13} are given by

$$B_{11} = -j\{(Y_{0ea} + Y_{0oa})\cot\Theta_a\}/2 \tag{7a}$$

$$B_{12} = -j\{(Y_{0ea} - Y_{0oa})\cot\Theta_a\}/2 \tag{7b}$$

$$B_{13} = j\{(Y_{0ea} - Y_{0oa})\csc\Theta_a\}/2 \tag{7c}$$

$$B_{14} = j\{(Y_{0ea} + Y_{0oa})\csc\Theta_a\}/2. \tag{7d}$$

The currents of i_1, i_2, i_3, and i_4 and the voltages of v_1, v_2, v_3, and v_4 in (6) should be identical to those in (7) at the design frequency, which leads to

$$B_{11} = \psi_2 = \phi_4 \tag{8a}$$

$$B_{12} = \psi_1 = \phi_3 \tag{8b}$$

$$B_{13} = \psi_4 = \phi_2 \tag{8c}$$

$$B_{14} = \psi_3 = \phi_1. \tag{8d}$$

The electrical length of Θ_a as well as the even- and odd-mode admittances of Y_{0ea} and Y_{0oa} in Fig. 3(b) or (f) can be easily calculated from (7) and (8), leading to

$$\cos\Theta_a = -\frac{B_{11}}{B_{14}} = -\frac{\psi_2}{\psi_3} \tag{9a}$$

$$Y_{0ea} = -j(B_{14} + B_{13})\sin\Theta_a = -j(\psi_3 + \psi_4)\sin\Theta_a \tag{9b}$$

$$Y_{0oa} = -j(B_{14} - B_{13})\sin\Theta_a = -j(\psi_3 - \psi_4)\sin\Theta_a. \tag{9c}$$

For the purpose of proof of concept, the asymmetric equivalent circuit in Fig. 3(b) was applied to the implementation of the 90° coupled transmission-line topology shown in Fig. 3(a) featuring a coupling coefficient of $C_0 = -3$ dB and assuming an all four-port termination to 50 Ω, leading to the calculated even- and odd-mode impedances $Z_{0eR} = 120.9$ Ω and $Z_{0oR} = 20.68$ Ω [12]. Based on these values of Z_{0eR} and Z_{0oR}, the even- and odd-mode impedances of $Z_{0ea} = Y_{0ea}^{-1}$ and $Z_{0oa} = Y_{0oa}^{-1}$, the electrical lengths of Θ_a and the coupling coefficient of C_a for the asymmetric equivalent

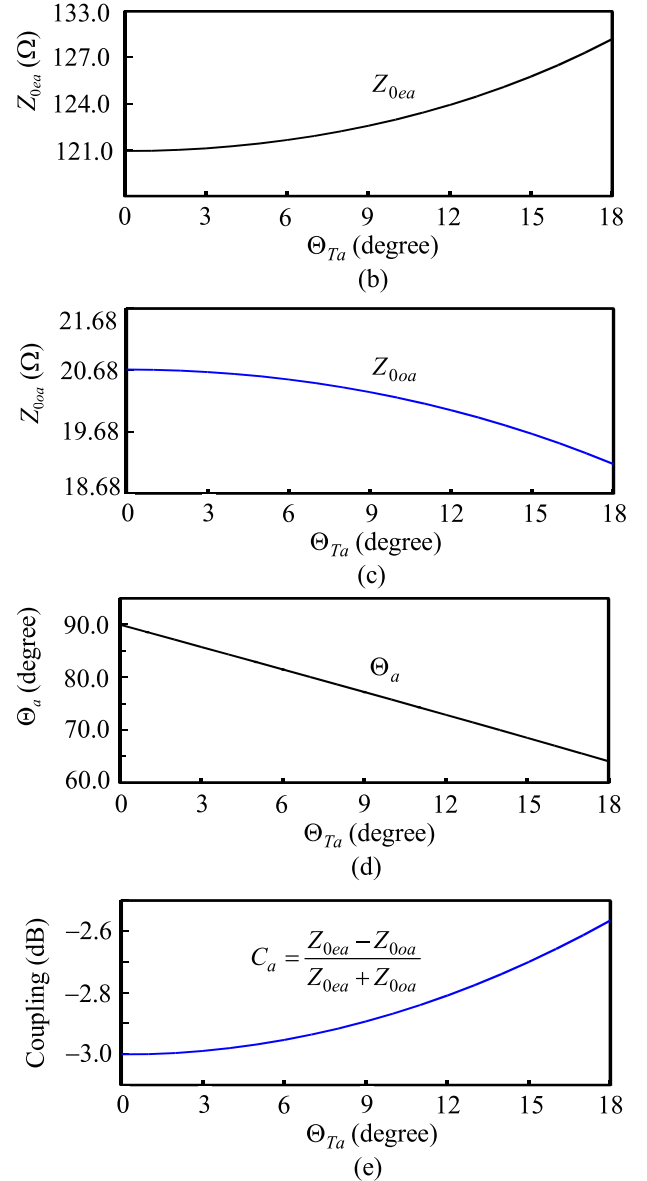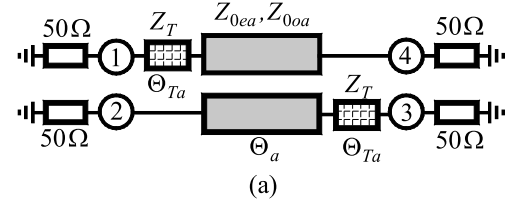

(a)

(b)

(c)

(d)

(e)

Fig. 5. Calculation results for an asymmetric equivalent circuit for the topology shown in Fig. 5(a) for different lengths Θ_{Ta} and a coupling coefficient of $C_0 = -3$ dB of the 90° coupled transmission-line sections in Fig. 3(a). (a) Asymmetric equivalent circuit topology. (b) Z_{0ea}. (c) Z_{0oa}. (d) Θ_a. (e) Coupling coefficient C_a.

circuit in Fig. 3(b) were calculated based on (9) by arbitrarily varying the electrical lengths of Θ_{Ta}. The calculation results are shown in Fig. 5 and listed in Table I.

When $\Theta_{Ta} = 0°$ in Fig. 5(a), the asymmetric equivalent circuit in Figs. 3(b) and 5(a) becomes identical to the 90° coupled transmission-line sections in Fig. 3(a). With the gradual increase in Θ_{Ta}, the values of Z_{0ea} increase as shown in

TABLE I
DESIGN DATA FOR Z_{0ea}, Z_{0oa}, AND Θ_a OF ASYMMETRIC EQUIVALENT
CIRCUIT WITH $Z_{0eR} = 120.9$ Ω AND $Z_{0oR} = 20.7$ Ω

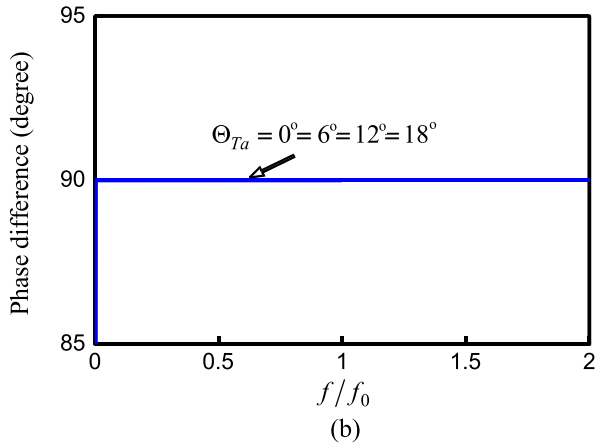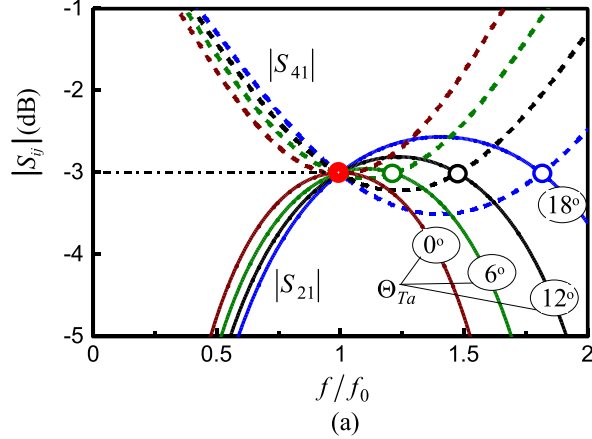| Θ_{Ta}	$Z_{0ea}(\Omega)$	$Z_{0oa}(\Omega)$	$\Theta_a(°)$
0°	120.90	20.70	90.00
3°	121.15	20.64	85.75
6°	121.87	20.51	81.49
9°	123.10	20.31	77.20
12°	124.90	20.02	72.88

(a)

(b)

Fig. 6. Frequency responses of the asymmetric equivalent circuit as a function of Θ_{Ta}. (a) Values of Coupled $|S_{21}|$ and Through of $|S_{41}|$. (b) Phase difference of $\angle S_{21} - \angle S_{41}$.

Fig. 5(b), while those of Z_{0oa} decrease as shown in Fig. 5(c), which leads to the gradual increase in the coupling coefficients of C_a, as shown in Fig. 5(e). The electrical lengths of Θ_a in Fig. 5(d) are inversely proportional to the electrical lengths of Θ_{Ta}. In Fig. 5(e), the coupling coefficient of C_a is equal to $C_0 = -3$ dB with $\Theta_{Ta} = 0°$ and features a gradual increase as a function of Θ_{Ta}.

To show the differences between the original one and its equivalent circuit in terms of frequency responses, four cases with $\Theta_{Ta} = 0°$, 6°, 12°, and 18° in Fig. 5(a) and Table I were simulated with ADS, a circuit simulator, and the frequency responses are shown in Fig. 6, where f_0 and f are the design and the operating frequencies. The scattering parameters of $|S_{41}|$ and $|S_{21}|$ of the asymmetric equivalent
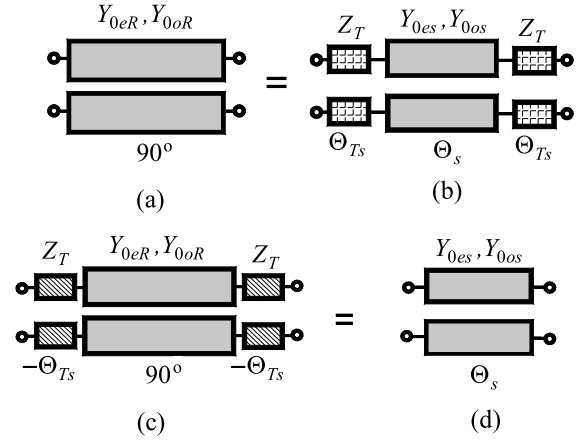

Fig. 7. Symmetric equivalent circuits. (a) 90° coupled transmission-line sections. (b) Symmetric equivalent circuit. (c) Adding four uncoupled transmission-line sections with $-\Theta_{Ts}$. (d) An equivalent set of coupled transmission-line sections with Y_{0es} and Y_{0os} and the electrical length of Θ_s.
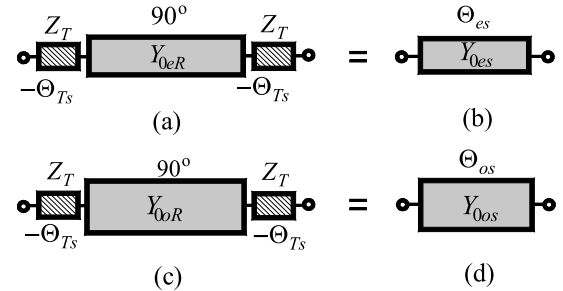

Fig. 8. (a) and (b) Even-mode equivalent circuits. (c) and (d) Odd-mode equivalent circuits.

circuit in Fig. 5(a) are shown in Fig. 6(a), while the phase difference of $\angle S_{21} - \angle S_{41}$ in Fig. 6(b). The two curves showing the frequency responses of $|S_{41}|$ and $|S_{21}|$ in Fig. 6(a) meet at the design frequency of f_0, regardless of the choice of Θ_{Ta}. When $\Theta_{Ta} = 0°$, the two responses meet only once at f_0, but those with $\Theta_{Ta} \neq 0°$ intersect at two frequencies, one of which is f_0 and the other is greater than f_0. That is, the bandwidths of $|S_{21}|$ increase with Θ_{Ta}. However, the phase responses of $\angle S_{21} - \angle S_{41}$ are, in any case, 90° in the frequency range of interest, as shown in Fig. 6(b).

B. Symmetric Equivalent Circuits

A set of 90° coupled transmission-line sections and its symmetric equivalent circuit are shown in Fig. 7, where the symmetric one in Fig. 7(b) consists of a set of coupled transmission-line sections and four identical uncoupled transmission-line sections. The even- and odd-mode admittances of the coupled-line sections of the symmetric equivalent circuit are Y_{0es} and Y_{0os}, and its electrical length is Θ_s. The characteristic impedance and the electrical length of the uncoupled transmission-line section in Fig. 7(b) are Z_T and Θ_{Ts}, respectively. To facilitate the calculations, the two circuits in Fig. 7(c) and (d) are similarly obtained by adding four transmission-line sections with $-\Theta_{Ts}$ to both circuits in Fig. 7(a) and (b). The two circuits in Fig. 7(c) and (d) are symmetric and therefore possible to analyze with even- and odd-mode excitations. The even- and odd-mode equivalent circuits are shown in Fig. 8.

TABLE II
DESIGN DATA FOR Z_{0es}, Z_{0os}, AND Θ_s OF SYMMETRIC EQUIVALENT CIRCUIT WITH $Z_{0eR} = 120.9 \ \Omega$ AND $Z_{0oR} = 20.7 \ \Omega$

Θ_{Ts}	$Z_{0es}(\Omega)$	$Z_{0os}(\Omega)$	$\Theta_s(°)$
0°	120.90 Ω	20.70 Ω	90.00
4°	122.63 Ω	20.39 Ω	78.64
6°	124.90 Ω	20.02 Ω	72.88
8°	128.35 Ω	19.48 Ω	67.03
10°	133.32 Ω	18.75 Ω	61.04

Considering the even-mode equivalent circuits in Fig. 8(a) and (b), the following relations yield:

$$jY_{0es}\tan\frac{\Theta_{es}}{2} = jY_T\frac{Y_{0eR} - Y_T\tan\Theta_{Ts}}{Y_T + Y_{0eR}\tan\Theta_{Ts}} = jE_{e\_s} \quad (10a)$$

$$-jY_{0es}\cot\frac{\Theta_{es}}{2} = -jY_T\frac{Y_{0eR} + Y_T\tan\Theta_{Ts}}{Y_T - Y_{0eR}\tan\Theta_{Ts}} = -jE_{o\_s}. \quad (10b)$$

From the odd-mode equivalent circuits in Fig. 8(c) and (d), the two equations in (11) are also obtained

$$jY_{0os}\tan\frac{\Theta_{os}}{2} = jY_T\frac{Y_{0oR} - Y_T\tan\Theta_{Ts}}{Y_T + Y_{0oR}\tan\Theta_{Ts}} = jO_{e\_s} \quad (11a)$$

$$-jY_{0os}\cot\frac{\Theta_{os}}{2} = -jY_T\frac{Y_{0oR} + Y_T\tan\Theta_{Ts}}{Y_T - Y_{0oR}\tan\Theta_{Ts}} = -jO_{o\_s}. \quad (11b)$$

The even- and odd-mode admittances of Y_{0es} and Y_{0os} in Fig. 8(b) and (d) can be calculated from (10) and (11) as

$$Y_{0es} = \sqrt{E_{e\_s}E_{o\_s}} \quad (12a)$$

$$Y_{0os} = \sqrt{O_{e\_s}O_{o\_s}}. \quad (12b)$$

The even-mode electrical length of Θ_{es} and the odd-mode electrical length of Θ_{os} in Fig. 8(b) and (d) are given by

$$\tan\frac{\Theta_{es}}{2} = \sqrt{\frac{E_{e\_s}}{E_{o\_s}}} \quad (13a)$$

$$\tan\frac{\Theta_{os}}{2} = \sqrt{\frac{O_{e\_s}}{O_{o\_s}}}. \quad (13b)$$

The average electrical length of Θ_s is

$$\Theta_s = \frac{\Theta_{es} + \Theta_{os}}{2}. \quad (14)$$

The three values in (13) and (14) are effectively the same, as the even- and odd-mode electrical lengths of the original 90° coupled transmission-line sections in Fig. 7(a) can be assumed to be the same due to their typically very small difference.

Based on the design equations in (12)–(14), the variables of the symmetric equivalent circuit were calculated for a proof-of-concept 3-dB directional coupler with the characteristic impedance of 50 Ω. The symmetric equivalent circuit with all 50-Ω termination impedances is shown in Fig. 9(a) and the values of the even- and odd-mode impedances of Z_{0es} and Z_{0os} are shown in Fig. 9(b) and (c), respectively, while the electrical lengths of Θ_s are shown in Fig. 9(d), and the
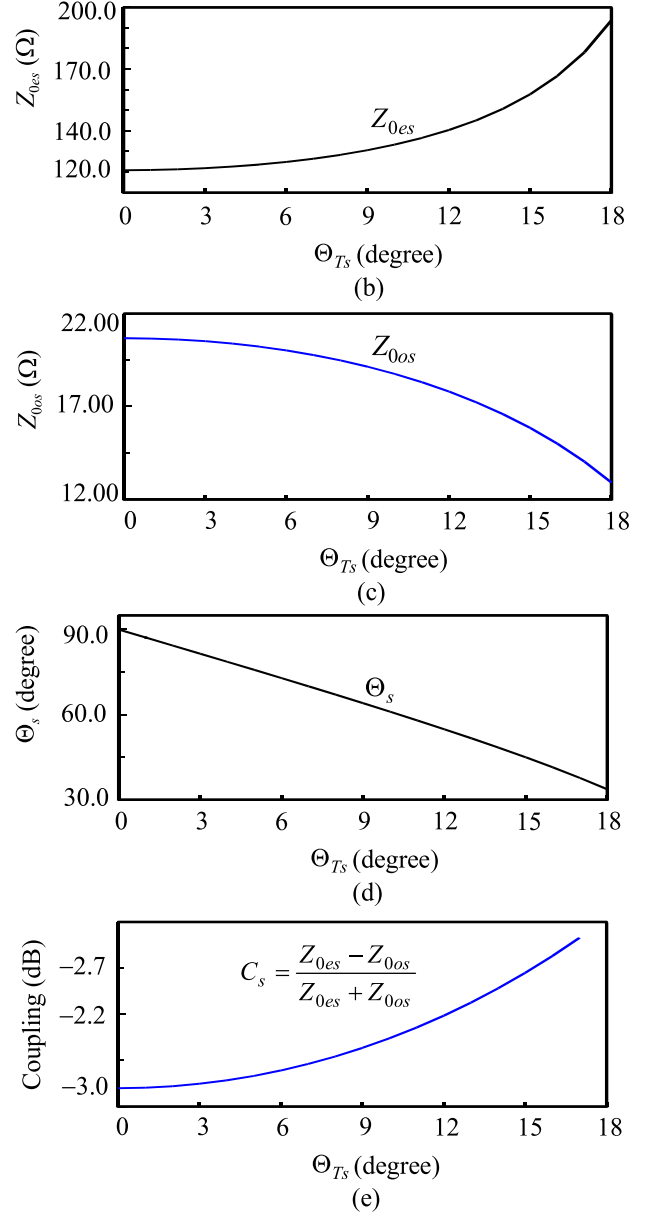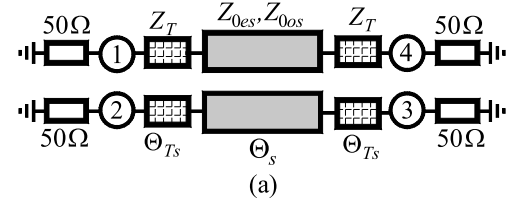

Fig. 9. Calculation results. (a) Symmetric equivalent circuit. (b) Z_{0es}. (c) Z_{0os}. (d) Θ_s. (e) Coupling coefficient C_s.

coupling coefficient C_s as a function of Z_{0es} and Z_{0os} is shown in Fig. 9(e). The design data for five cases of different values of Θ_{Ts} are also listed in Table II. When $\Theta_{Ts} = 0°$, the equivalent circuit in Fig. 9(a) is the same as the 90° 3-dB directional coupler in Fig. 7(a). With the gradual increase in Θ_{Ts} in Fig. 9, the values of Z_{0es} increase as shown in Fig. 9(b), but those of Z_{0os} decrease as demonstrated in Fig. 9(c), leading to coupling coefficients of C_s higher than −3 dB.

The frequency responses of the four cases with $\Theta_{Ts} = 0°$, 4°, 6°, and 8° in Table II were simulated, and the simulation
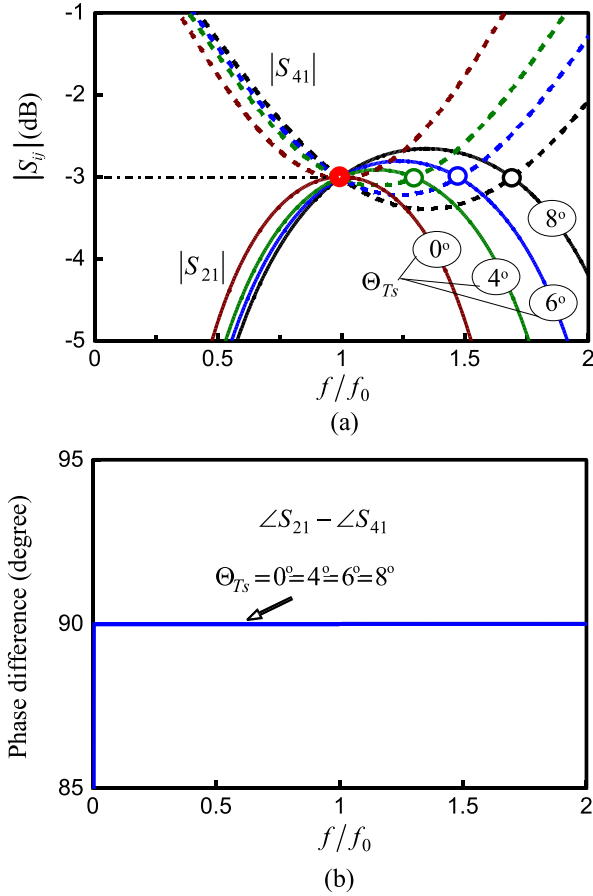
Fig. 10. Frequency responses of the symmetric equivalent circuit as a function of Θ_{Ts}. (a) Values of Coupled $|S_{21}|$ and Through $|S_{41}|$. (b) Phase difference of $\angle S_{21} - \angle S_{41}$.

results are shown in Fig. 10, where the responses of $|S_{21}|$ and $|S_{41}|$ are shown in Fig. 10(a), and the phase responses of $\angle S_{21} - \angle S_{41}$ in Fig. 10(b). The frequency responses of the symmetric equivalent circuits are very similar to those of the asymmetric ones in Fig. 6.

C. Mixed Equivalent Circuits

The mixed equivalent circuit is shown in Fig. 11(a) and consists of one set of coupled transmission-line sections with the even- and odd-mode admittances of Y_{0em} and Y_{0om} and with the electrical length of Θ_m, and four uncoupled transmission-line sections. The characteristic admittances of all four uncoupled transmission-line sections are the same as Y_T with two located diagonally being $\Theta_{Ts} + \Theta_{Ta}$ long, while two others are Θ_{Ts} long. The mixed topology in Fig. 11(a) may be changed to that in Fig. 11(b) where the circuit in the dashed rectangle is a symmetric coupled transmission-line topology, leading to the asymmetric equivalent circuit, as shown in Fig. 11(c).

Therefore, the design formulas for Y_{0em}, Y_{0om}, and Θ_{Tm} can be derived by equating the admittance parameters of the circuit in the dashed rectangle in Fig. 11(b) to those of the coupled transmission-line sections with Z_{0ea}, Z_{0oa}, and Θ_a in Fig. 11(c). In a way similar to the symmetric equivalent circuit, the relations in Fig. 12 are derived. The dashed rectangle part in Fig. 11(b) is again shown in
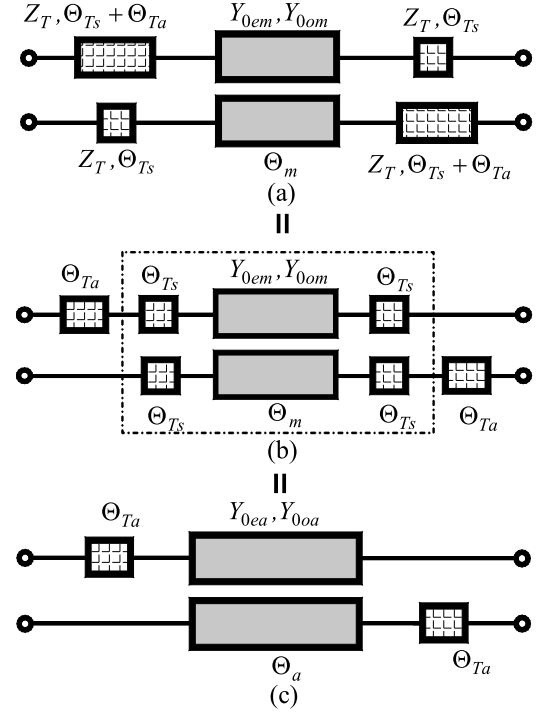

Fig. 11. Mixed equivalent circuit. (a) Mixed one with four transmission-line sections. (b) Mixed one with six transmission-line sections. (c) Asymmetric equivalent circuit with Θ_{Ta}.

Fig. 12(a), which is equivalent to a set of coupled transmission-line sections with Y_{0ea}, Y_{0oa}, and Θ_a in Fig. 12(b). By adding four uncoupled transmission lines of negative length $-\Theta_{Ts}$, the set of coupled transmission-line sections with Y_{0em}, Y_{0om}, and Θ_m in Fig. 12(c) can be equivalent to the circuit with Y_{0ea}, Y_{0oa}, Θ_a, and $-\Theta_{Ts}$ in Fig. 12(d). All topologies in Fig. 12 are symmetric, and therefore, even- and odd-mode excitation analyses may be applied, from which the following equations are obtained:

$$jY_{0em}\tan\frac{\Theta_{em}}{2} = jY_T\frac{Y_{0ea}\tan\frac{\Theta_a}{2} - Y_T\tan\Theta_{Ts}}{Y_T + Y_{0ea}\tan\frac{\Theta_a}{2}\tan\Theta_{Ts}}$$
$$= jE_{e\_m} \tag{15a}$$

$$-jY_{0em}\cot\frac{\Theta_{em}}{2} = -jY_T\frac{Y_{0ea}\cot\frac{\Theta_a}{2} + Y_T\tan\Theta_{Ts}}{Y_T - Y_{0ea}\cot\frac{\Theta_a}{2}\tan\Theta_{Ts}}$$
$$= -jE_{o\_m} \tag{15b}$$

$$jY_{0om}\tan\frac{\Theta_{om}}{2} = jY_T\frac{Y_{0oa}\tan\frac{\Theta_a}{2} - Y_T\tan\Theta_{Ts}}{Y_T + Y_{0oa}\tan\frac{\Theta_a}{2}\tan\Theta_{Ts}}$$
$$= jO_{e\_m} \tag{15c}$$

$$-jY_{0om}\cot\frac{\Theta_{om}}{2} = -jY_T\frac{Y_{0oa}\cot\frac{\Theta_a}{2} + Y_T\tan\Theta_{Ts}}{Y_T - Y_{0oa}\cot\frac{\Theta_a}{2}\tan\Theta_{Ts}}$$
$$= -jO_{o\_m}. \tag{15d}$$

The even- and odd-mode admittances of Y_{0em} and Y_{0om} in Figs. 11 and 12 are found from (15) such as

$$Y_{0em} = \sqrt{E_{e\_m}E_{o\_m}} \tag{16a}$$

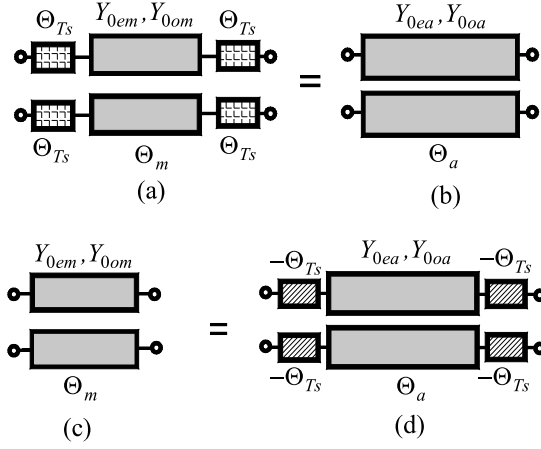$$Y_{0om} = \sqrt{O_{e\_m}O_{o\_m}}. \tag{16b}$$

Fig. 12. Relations among mixed, asymmetric, and symmetric equivalent circuits. (a) Dashed rectangle part in Fig. 11(b) with Y_{0em}, Y_{0om}, and Θ_m. (b) Set of coupled transmission-line sections with Y_{0ea}, Y_{0oa}, and Θ_a. (c) Set of coupled transmission-line sections with Y_{0em}, Y_{0om}, and Θ_m. (d) Symmetric equivalent circuit with Y_{0ea}, Y_{0oa}, and Θ_a.

TABLE III

DESIGN DATA FOR Z_{0em}, Z_{0om}, AND Θ_m OF MIXED EQUIVALENT CIRCUIT WITH $Z_{0eR} = 120.9\ \Omega$ AND $Z_{0oR} = 20.7\ \Omega$ AND $\Theta_{Ta} = 5°$ FIXED

Θ_{Ts}	$Z_{0em}(\Omega)$	$Z_{0om}(\Omega)$	$\Theta_m(°)$
0°	121.57	20.56	82.91
2°	123.10	20.31	77.20
4°	125.64	19.90	71.43
6°	129.43	19.32	65.55
8°	134.86	18.54	59.51

The even-mode electrical length of Θ_{em} and the odd-mode electrical length of Θ_{om} in Fig. 12 are given by

$$\tan\frac{\Theta_{em}}{2} = \sqrt{\frac{E_{e\_m}}{E_{o\_m}}} \tag{17a}$$

$$\tan\frac{\Theta_{om}}{2} = \sqrt{\frac{O_{e\_m}}{O_{o\_m}}}. \tag{17b}$$

The average electrical length of Θ_m is

$$\Theta_m = \frac{\Theta_{em} + \Theta_{om}}{2}. \tag{18}$$

The three values in (17) and (18) are effectively the same similarly to the symmetric equivalent circuit case.

Based on the design formulas in (16)–(18), the design data for the mixed equivalent circuit in Fig. 11(a) were calculated for a proof-of-concept 90° 3-dB directional coupler with the characteristic impedance of 50 Ω. The values of the even- and odd-mode impedances of Z_{0em} and Z_{0om} and the electrical length of Θ_m are listed in Table III for five different values of Θ_{Ts} and a fixed Θ_{Ta} of 5°.

The frequency responses of the four cases in Table III are shown in Fig. 13 where the responses of $|S_{21}|$ and $|S_{41}|$ are in Fig. 13(a) and the phase responses of $\angle S_{21} - \angle S_{41}$ in Fig. 13(b). In any case, the four mixed equivalent circuits are
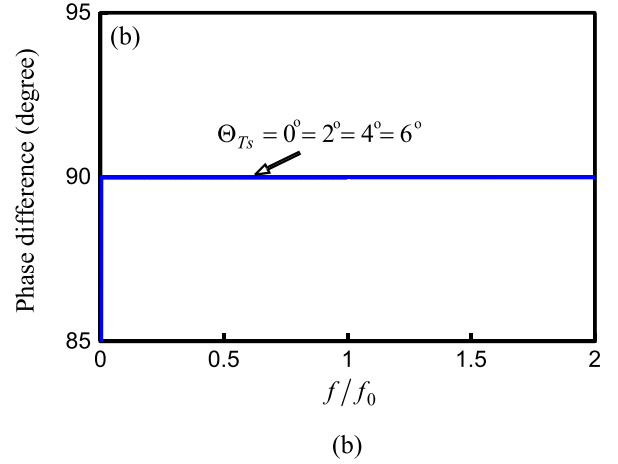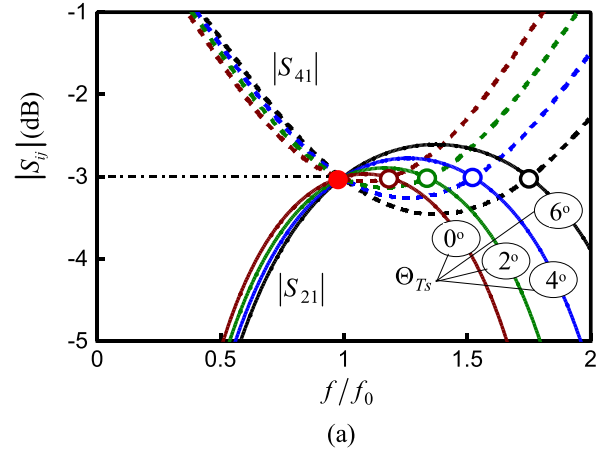

(a)

(b)

Fig. 13. Frequency responses of the mixed equivalent circuit with $\Theta_{Ta} = 5°$ fixed. (a) Values of Coupled $|S_{21}|$ and Through $|S_{41}|$. (b) Phase difference of $\angle S_{21} - \angle S_{41}$.

perfectly matched at f_0 and the bandwidths increase gradually with Θ_{Ts}. The phase differences of $\angle S_{21} - \angle S_{41}$ in Fig. 13(b) show a constant 90°, regardless of the Θ_{Ts}.

When Y_{0eR} and Y_{0oR} of the 90° coupled transmission-line sections are given, the required condition for the equal lengths of all three equivalent circuits $\Theta_a = \Theta_s = \Theta_m$ becomes

$$\Theta_{Ta} \text{ for asymmetric} = 2\Theta_{Ts} \text{ for symmetric}$$
$$= (2\Theta_{Ts} + \Theta_{Ta}) \text{ for mixed.} \tag{19}$$

III. APPLICATIONS TO MARCHAND BALUN DESIGNS

The asymmetric, symmetric, and mixed equivalent circuits in Figs. 3(b), 7(b), and 11(a) can be substituted for the two 90° coupled transmission-line sections of the Marchand baluns with the connecting segments. The case with the asymmetric ones will be first investigated for arbitrary impedance termination values as a proof-of-concept demonstration.

Changing the locations of the uncoupled transmission-line sections of each asymmetric equivalent circuit, three cases of the connecting segments are possible, one of which is shown in Fig. 14(a) and its isolation circuit is in Fig. 14(b). The termination impedance at port ① is R_r and that at ports ② and ③ R_L, as shown in Fig. 14(a). The isolation
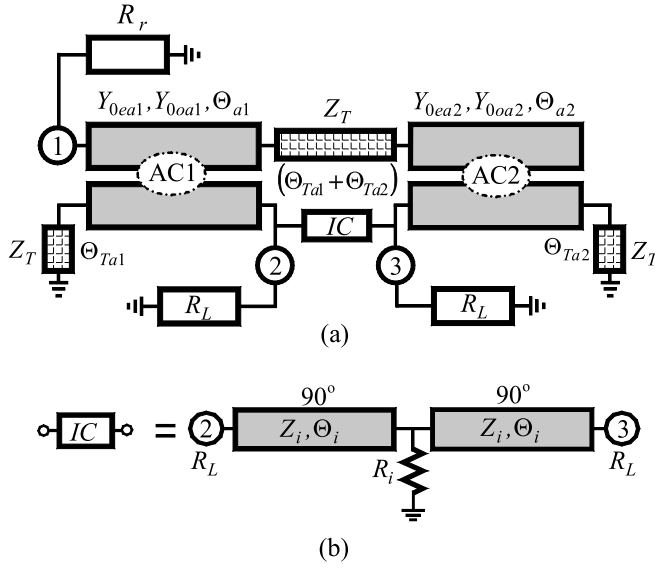
Fig. 14. Impedance-transforming Marchand balun with the connecting segment. (a) Marchand balun. (b) Isolation circuit.

circuit is composed of two 90° identical transmission-line sections with the characteristic impedance of Z_i and an isolation resistance of R_i. For a better understanding, the asymmetric equivalent circuit connected at port ① is termed AC1, while that connected at port ③ AC2. The even- and odd-mode admittances and the electrical length of the AC1 are Y_{0ea1}, Y_{0ea1}, and Θ_{a1}. The electrical length of the uncoupled transmission-line sections of the AC1 is Θ_{Ta1}. Those of the AC2 are Y_{0ea2}, Y_{0ea2}, Θ_{a2}, and Θ_{Ta2}, and the characteristic impedances of the uncoupled transmission-line sections are equal to Z_T. The connecting segment can be assumed to be the superposition of the two uncoupled transmission line sections with a total length of $\Theta_{Ta1} + \Theta_{Ta2}$, thus enabling its accurate simulation and modeling.

The design formulas for Z_{0eR} and Z_{0oR} with $\Theta_{a1} = \Theta_{a2} = 90°$ in Fig. 14(a) [5, eq. (9)] are

$$Z_{0eR} = \sqrt{2 R_r R_L} \frac{C_0}{1 - C_0} \tag{20a}$$

$$Z_{0oR} = \sqrt{2 R_r R_L} \frac{C_0}{1 + C_0}. \tag{20b}$$

Substituting $R_r = R_L = 50\ \Omega$ and $C_0 = -4.77$ dB into (20) gives $Z_{0eR} = 96.62\ \Omega$ and $Z_{0oR} = 25.88\ \Omega$, which gives $Z_T = 50\ \Omega$. For the case, when $\Theta_{Ta1} = \Theta_{Ta2} = 21.5°$ in Fig. 14(a), the electrical lengths of Θ_{a1} and Θ_{a2} are, referring to (9a), calculated as $\Theta_{a1} = \Theta_{a2} = 63.33°$, being about the same as that in [9, Fig. 9(a)], featuring a $C_0 = -4.8$ dB. When $\Theta_{Ta1} = 23°$ and $\Theta_{Ta2} = 0°$, the electrical lengths of $\Theta_{a1} = 61.41°$ and $\Theta_{a2} = 90°$ are calculated, being the same as those in [9, Fig. 7(a)]. That is, the conventional design [9] is effective only for the case of $Z_T = R_r = R_L = 50\ \Omega$ and $C_0 = -4.77$ dB.

Based on the design equations in (20), the Marchand baluns terminated in $R_r = 50\ \Omega$ and $R_L = 100\ \Omega$ were also simulated by fixing the coupling coefficient of $C_0 = -4$ dB and varying the electrical lengths of the uncoupled

TABLE IV
DESIGN DATA FOR THE MARCHAND BALUNS WITH ASYMMETRIC EQUIV-ALENT CIRCUITS WHEN $R_r = 50\ \Omega$, $R_L = 100\ \Omega$, AND $C_0 = -4$ dB

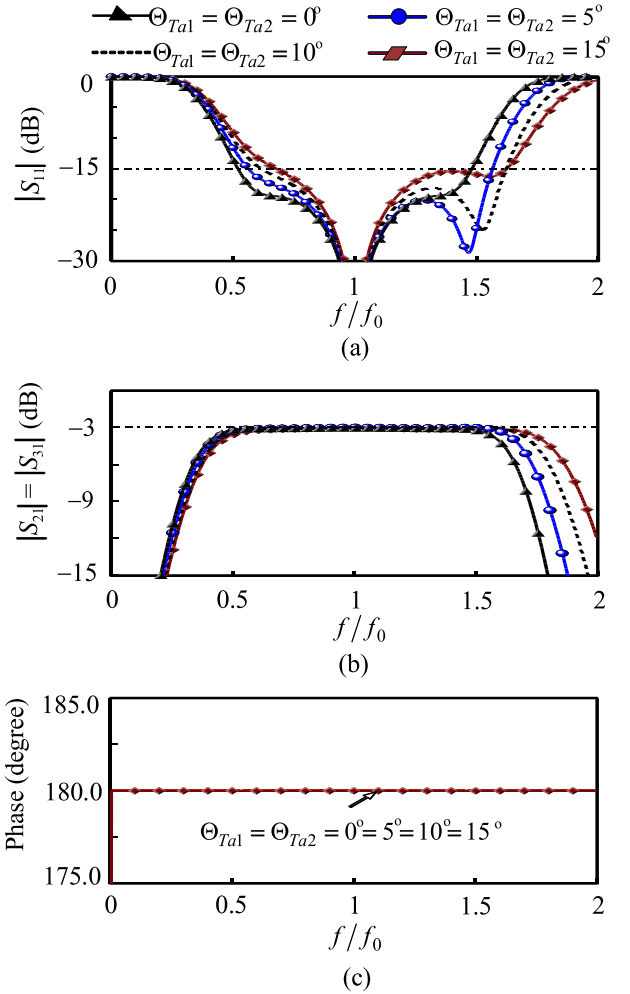| Θ_{Ta1} $= \Theta_{Ta2}$	Z_{0ea1} $= Z_{0ea2}$	Z_{0oa1} $= Z_{0oa2}$	$\Theta_{a1} = \Theta_{a2}$
0°	170.97 Ω	38.69 Ω	90.00°
5°	171.66 Ω	38.53 Ω	83.55°
10°	173.79 Ω	38.06 Ω	77.07°
15°	177.57 Ω	37.25 Ω	70.51°
20°	183.44 Ω	36.06 Ω	63.84°

Fig. 15. Simulation results of the Marchand balun with $\Theta_{Ta1} = \Theta_{Ta2}$. (a) $|S_{11}|$. (b) $|S_{21}| = |S_{31}|$. (c) Phase differences of $|\angle S_{21} - \angle S_{31}|$.

transmission line sections under the simplifying assumption of $\Theta_{Ta1} = \Theta_{Ta2}$. In this case, $Z_{0eR} = 170.97\ \Omega$ and $Z_{0oR} = 38.69\ \Omega$, which gives $Z_T = 81.33\ \Omega$. The design data for $Z_{0ea1} = Z_{0ea2}$, $Z_{0oa1} = Z_{0oa2}$, and $\Theta_{a1} = \Theta_{a2}$ are listed in Table IV, based on which the frequency responses are shown in Fig. 15 where the responses of $|S_{11}|$ at port ① are in Fig. 15(a), the power divisions of $|S_{21}|$ and $|S_{31}|$ in Fig. 15(b), and the phase differences of $|\angle S_{21} - \angle S_{31}|$ in Fig. 15(c).

For the values of $\Theta_{Ta1} = \Theta_{Ta2} = 0°$, the Marchand balun in Fig. 14(a) becomes the conventional one [5], and the matching response of $|S_{11}|$ is symmetric with respect to the design frequency of f_0. When $\Theta_{Ta1} = \Theta_{Ta2}$ is greater than $0°$, the frequency responses of $|S_{11}|$ are not any more symmetric, and additional ripples are generated at the frequencies greater than f_0, an effect that can be explained considering Fig. 6(a) demonstrating that the frequency responses of $|S_{41}|$ and $|S_{21}|$ meet only at f_0 when $\Theta_T = 0°$ but at two frequencies with $\Theta_T \neq 0°$. In a similar principle, the ripples in Fig. 15(a) are available when $\Theta_{Ta1} = \Theta_{Ta2} \neq 0°$. The power divisions of $|S_{21}|$ and $|S_{31}|$ feature the identical frequency responses in Fig. 15(b) as far as $\Theta_{T1} = \Theta_{T2}$, and the phase difference between the two output ports in Fig. 15(c) is $180°$ throughout the whole frequency range of interest.

On the other hand, in [11, Fig. 3] where the termination impedances are the same with the values of $R_r = 50\ \Omega$ and $R_L = 10\ \Omega$, and the coupling coefficient of C_0 is -3 dB, the perfect matching does not appear at f_0 and the phase differences between the two outputs are not $180°$ any more around $1.8f_0$–$2f_0$ when the connecting segments are included in the simulations. The degradation in the phase difference may be due to the fact that the two sets of coupled transmission-line sections in [11, Fig. 2(c)] perform differently due to the lack of any phase compensation loads (uncoupled transmission line section) similar to the ones introduced in this paper (with the characteristic impedance Z_T and lengths Θ_{Ta1} or Θ_{Ta2}) in Fig. 14 or [9, Fig. 2(a)], an issue that will be further verified with the following example of $\Theta_{Ta1} \neq \Theta_{Ta2}$.

Even with $\Theta_{Ta1} \neq \Theta_{Ta2}$, the circuit in Fig. 14(a) may be employed in baluns, but the frequency performance does not seem to be desirable. The frequency responses of the Marchand balun in Fig. 14(a) without the isolation circuit were simulated with $\Theta_{Ta1} = 0°$ fixed and Θ_{Ta2} varying, and the simulation results are shown in Fig. 16 where the power-division ratios of (S_{21}/S_{31}) are shown in Fig. 16(a), while the phase difference of $|\angle S_{21} - \angle S_{31}|$ and the matching $|S_{11}|$ at port ① are shown in Fig. 16(b) and (c), respectively.

When $\Theta_{Ta1} = \Theta_{Ta2} = 0°$, a unity power-division ratio in Fig. 16(a) and $180°$ phase difference of $|\angle S_{21} - \angle S_{31}|$ in Fig. 16(b) are achieved over the whole frequency range of interest. When $\Theta_{Ta1} = 0°$ and $\Theta_{Ta2} \neq 0°$, a unity power-division ratio and $180°$ phase difference of $|\angle S_{21} - \angle S_{31}|$ are achieved only at f_0, and the deviation is bigger as the difference between Θ_{Ta1} and Θ_{Ta2} is larger. From the simulation results in Figs. 15 and 16, Θ_{Ta1} should be the same as Θ_{Ta2} for an effective balun performance. Even with $\Theta_{Ta1} \neq \Theta_{Ta2}$, the perfect matching is, in any case, achieved at f_0 in Fig. 16(c) with the equivalent circuit proposed in this paper, contrary to the case shown in [11, Fig. 3] that fails to achieve near-perfect matching for any length of the connecting section.

For the sake of completeness, the symmetric and the mixed equivalent circuits were also applied to the simulation of the same (Table IV) Marchand balun configuration with $R_r = 50\ \Omega$, $R_L = 100\ \Omega$, $Z_{0eR} = 170.97\ \Omega$, and $Z_{0oR} = 38.69\ \Omega$. The values of $\Theta_{Ts} = 6°$ for the symmetric equivalent circuit and $\Theta_{Ta} = 10°$ and $\Theta_{Ts} = 6°$ for the mixed one were

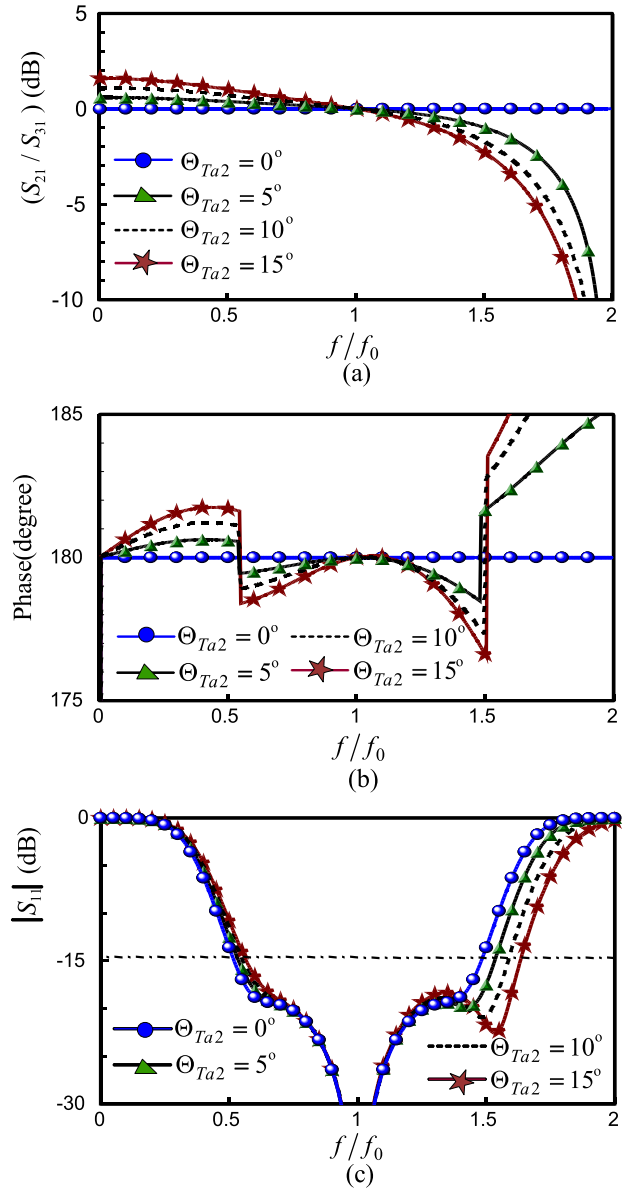Fig. 16. Simulation results of the Marchand balun with $\Theta_{Ta1} \neq \Theta_{Ta2}$, $\Theta_{Ta1} = 0°$. (a) S_{21}/S_{31}. (b) Phase difference of $|\angle S_{21} - \angle S_{31}|$. (c) $|S_{11}|$.

TABLE V
DESIGN DATA FOR MARCHAND BALUNS WITH SYMMETRIC AND MIXED EQUIVALENT CIRCUITS WHEN $R_r = 50\ \Omega$, $R_L = 100\ \Omega$, AND $C_0 = -4$ dB

Symmetric equivalent circuit ($\Theta_{Ts} = 6°$)
$Z_{0es} = 175.09\ \Omega$, $Z_{0os} = 37.78\ \Omega$, and $\Theta_s = 74.46°$
Mixed equivalent circuit ($\Theta_{Ta} = 10°$, $\Theta_{Ts} = 6°$)
$Z_{0em} = 186.52\ \Omega$, $Z_{0om} = 35.46\ \Omega$, and $\Theta_m = 61.13°$

selected arbitrarily. The design data are listed in Table V, based on which the two respective Marchand baluns were simulated with the same $90°$ directional couplers. The simulation results are shown in Fig. 17 where the frequency responses of $|S_{11}|$ are shown in Fig. 17(a), while those of
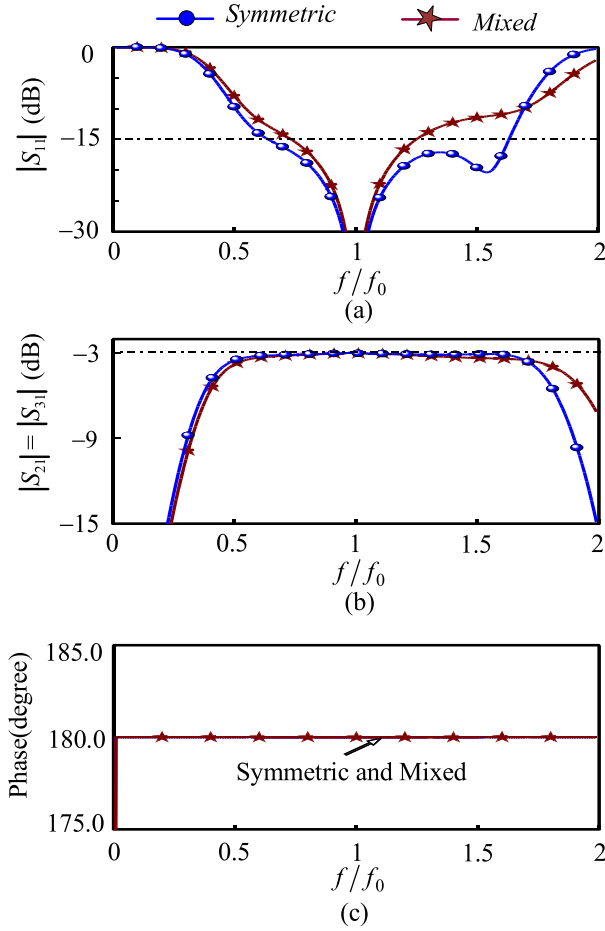
Fig. 17. Simulation results of the Marchand baluns with the symmetric and mixed equivalent circuits. (a) $|S_{11}|$. (b) $|S_{21}| = |S_{31}|$. (c) Phase differences of $|\angle S_{21} - \angle S_{31}|$.

$|S_{21}| = |S_{31}|$ and the phase differences of $|\angle S_{21} - \angle S_{31}|$ in Fig. 17(b) and (c), respectively, featuring a very good (near-ideal) performance in terms of all three parameters.

IV. EXPERIMENTAL VERIFICATION

To verify the suggested theory, the symmetric and the asymmetric equivalent circuits were fabricated on the substrate (RT/duroid 5870, $\varepsilon_r = 2.33$, and $H = 31$ mil) for the implementation of 90° coupled transmission-line sections as well as of a Marchand balun.

A. 3-D Structure

A proof-of-concept topology of two coupled microstrip transmission-line sections (2-D structure) is shown in Fig. 18(a), and the gap between the two conductors, Con-1 and Con-2, is fixed at 20 mil to allow for an easy fabrication. The even- and odd-mode impedances of 2-D structure are

$$Z'_{0e} = \frac{\sqrt{\varepsilon'_{\text{eff}}\mu}}{C_{11}} \qquad Z'_{0o} = \frac{\sqrt{\varepsilon'_{\text{eff}}\mu}}{C_{11} + 2C_{12}} \qquad (21)$$

where $C_{11} = C_{22}$ due to the same widths of w_c in Fig. 18(a), $\varepsilon'_{\text{eff}}$ and μ are the effective permittivity and permeability of the
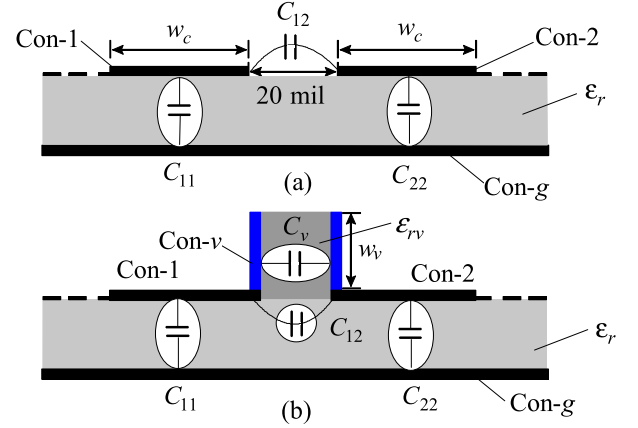

Fig. 18. 2-D and 3-D coupled transmission-line sections. (a) 2-D structure. (b) 3-D structure.

substrate with the dielectric constant of ε_r, and C_{11} and C_{12} are the capacitances shown in Fig. 18(a).

A tight coupling higher than -5 dB is difficult to achieve with the 2-D structure and therefore, the 3-D structure with the VIP (vertically installed planar structure) on a substrate with ε_{rv} in Fig. 18(b) is necessary. In this case of the 3-D structure, the even-mode impedance of Z_{0e} may be assumed to be the same as Z'_{0e}, because the electrical fields are mainly confined within the substrate with ε_r for an even-mode excitation. The odd-mode impedance of Z_{0o} of the 3-D structure can be expressed in a way similar to (21) as

$$\frac{1}{Z_{0o}} = \frac{C_{11} + 2C_{12}}{\sqrt{\varepsilon'_{\text{eff}}\mu}} + \frac{2C_v}{\sqrt{\varepsilon_{\text{eff}}\mu}} \qquad (22)$$

where ε_{eff} is the effective permittivity of the VIP for the odd-mode excitation. Combining (21) and (22) leads to the following expression for the capacitance $2C_v$ in Fig. 18(b):

$$\frac{2C_v}{\sqrt{\varepsilon_{\text{eff}}\mu}} = \left(\frac{1}{Z_{0o}} - \frac{1}{Z'_{0o}}\right) \qquad (23)$$

where $Z_{0e} \approx Z'_{0e}$ is assumed, and Z_{0o} and Z'_{0o} are the odd-mode impedances of the 3-D and 2-D structures, respectively.

B. Symmetric Equivalent Circuit

Using the symmetric coupled line configuration in Fig. 9(a), the coupled-line topology with $\Theta_{Ts} = 8°$, that is listed in Table II, was fabricated on the specified substrate using the 3-D structure for the coupled line sections. In this case, $Z_{0es} = 128.35$ Ω, $Z_{0os} = 19.48$ Ω, and $\Theta_s = 67.03°$ and the design frequency was chosen to be 2 GHz. In order to build the 3-D topology satisfying the coupler design parameters, the 2-D structure dimensions have to be first determined for the required Z'_{0es} on the given substrate. Fixing the gap at 20 mil in Fig. 18(a) in order to realize the required $Z'_{0es} = 128.35$ Ω, the value of $w_c = 0.57$ mm in Fig. 18(a) is obtained through ADS simulations (everybody knows it).

In this case, $Z'_{0es} = 128.35$ Ω and $Z'_{0os} = 78.551$ Ω, with which $2C_v$ is calculated as $\sqrt{\varepsilon_{\text{eff}}\mu}/25.9$ from (23). That is, the impedance produced by the VIP should be 25.9 Ω with the odd-mode excitation. As the dominant mode of the VIP section
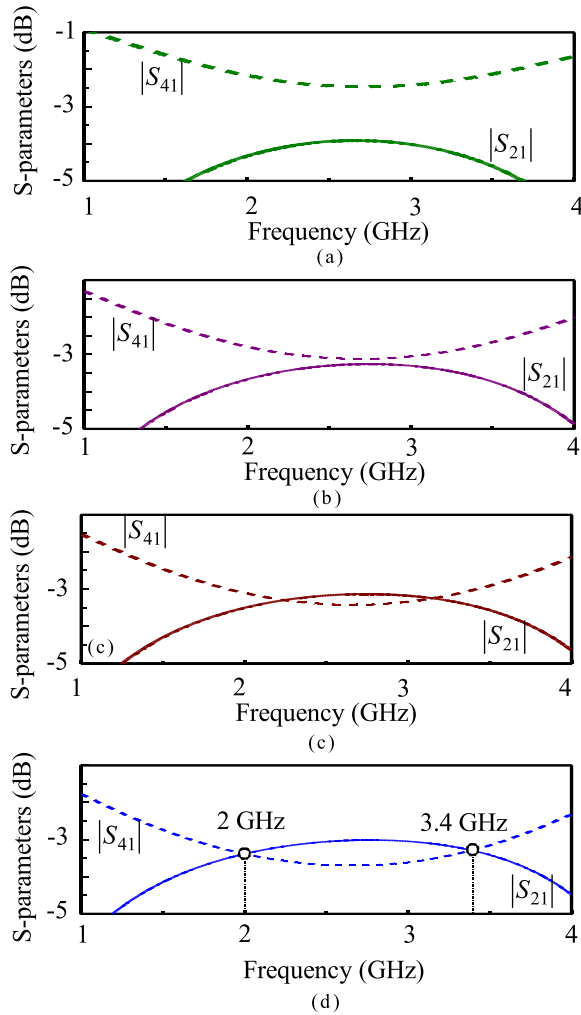
Fig. 19. Coupling ($|S_{21}|$) variations as a function of the VIP length w_v. (a) $w_v = 1.85$ mm. (b) $w_v = 2.5$ mm. (c) $w_v = 3$ mm. (b) $w_v = 3.45$ mm.

can be approximated by the parallel-plate TEM mode, various values of w_v in Fig. 18(b) were investigated using Ansys HFSS to achieve this value of 25.9 Ω, as shown in Fig. 19, with an optimal value around 3.45 mm for $\varepsilon_r = \varepsilon_{rv} = 2.33$ in Fig. 18(b).

When the length of w_v is 1.85 mm in Fig. 19(a), the coupling is only -4.32 dB at 2 GHz. When $w_v = 3$ mm in Fig. 19(c), the two curves meet at two frequencies, but the coupling is not sufficient yet. When $w_v = 3.45$ mm in Fig. 19(d), the two curves meet at two frequencies, 2 and 3.4 GHz, but the coupling is less than -3 dB at 2 GHz, because the real materials with conductor and dielectric losses were considered for the simulations. Considering that the design frequency is 2 GHz, the results in Fig. 19(d) are the same with those in Fig. 10(a) with $\Theta_{Ts} = 8°$. In this way, all the required physical dimensions may be determined and their values are listed in Table VI, where w_t and L_t are the width and length of the uncoupled transmission-line sections with Z_T and Θ_{Ts}, while w_c, g, and L_c are the width, the gap, and the length of the coupled transmission-line sections, and w_v is the length of the VIP in Fig. 18(b).

The fabricated symmetric circuit prototype is shown in Fig. 20(a) and the results measured and simulated by
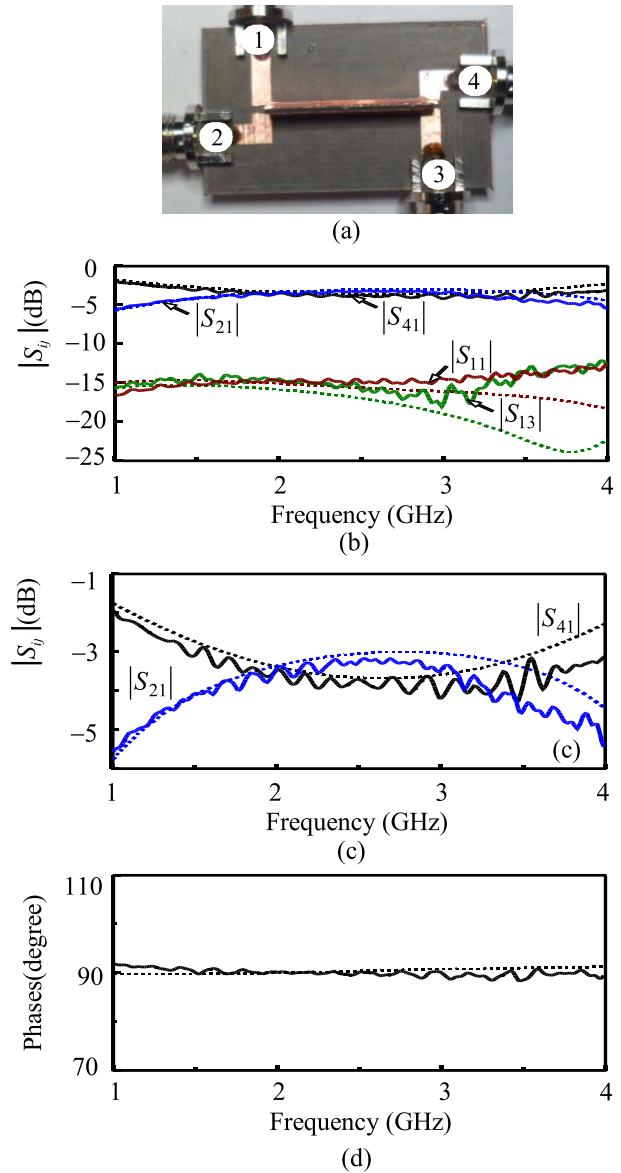

Fig. 20. Symmetric fabricated equivalent circuit along with the measured (solid lines) and predicted results (dotted lines). (a) Fabricated circuit. (b) Scattering parameters from port ①. (c) $|S_{21}|$ and $|S_{41}|$. (d) Phase difference between S_{21} and S_{41}.

TABLE VI
DESIGN AND FABRICATION DATA FOR SYMMETRIC EQUIVALENT CIRCUIT

Design data	$Z_{0es} = 128.35$ Ω, $Z_{0os} = 19.48$ Ω, $\Theta_s = 67.03°$, $Z_T = 50$ Ω, $\Theta_{Ts} = 8°$.
Fabrication dimensions (mm)	$w_t = 2.35$, $L_t = 2.4$, $w_c = 0.57$, $g = 0.51$, $L_c = 20.5$, $w_v = 3.45$

the 3-D full wave simulator HFSS are compared in Fig. 20(b)–(d) where matching at port ① $|S_{11}|$, coupled $|S_{21}|$, isolation of $|S_{31}|$ and through of $|S_{41}|$ are shown in Fig. 20(b), with only $|S_{21}|$ and $|S_{41}|$ being expanded in Fig. 20(c), and the phase difference between S_{21} and S_{41} in Fig. 20(d). The measured

TABLE VII

DESIGN AND FABRICATION DATA FOR
ASYMMETRIC EQUIVALENT CIRCUIT

Design data	$Z_{0ea} = 104.5\ \Omega,\ \ Z_{0oa} = 16.75\ \Omega,$ $\Theta_a = 72.88^o, Z_T = 41.83\ \Omega, \Theta_{Ta} = 12^o.$
Fabrication dimensions (mm)	$w_t = 3.06, L_t = 3.57, w_c = 0.87,$ $g = 0.51, L_c = 22.5, w_v = 3.75$

results of the scattering parameters at 2 GHz are $|S_{21}| = -3.42$ dB $|S_{41}| = -3.49$ dB, $|S_{11}| = -14.85$ dB, and $|S_{31}| = -14.59$ dB. The phase difference between S_{21} and S_{41} is 91.33° at 2 GHz.

C. Asymmetric Equivalent Circuit

Using the asymmetric circuit, an impedance-transforming (35 into 50 Ω) directional coupler was designed at 2 GHz. In this case, when $C_0 = -3$ dB is chosen, $Z_{0eR} = 101.16\ \Omega$ and $Z_{0oR} = 17.3\ \Omega$ are calculated [12]. If $\Theta_{Ta} = 12°$ is chosen, $Z_{0ea} = 104.5\ \Omega$, $Z_{0oa} = 16.75\ \Omega$, and $\Theta_a = 72.88°$ are calculated, which gives $Z_T = 41.83\ \Omega$. The fabrication dimensions may be obtained in a similar way to Section IV-B and are listed in Table VII.

The fabricated circuit prototype is shown in Fig. 21(a). The real termination impedances at ports ① and ② are 35 Ω, but the fabricated feeding lines are of 50-Ω characteristic impedances for the measurements. After deembedding the feeding line effect from the measured results, they were simulated once more with the correct termination impedances (35 Ω and 50 Ω), which gives wanted measurements requiring their deembedding from the measured results. In this case, since the termination impedances are different from each other, the simulated results are not the same as those in Fig. 6 and the bandwidth is slightly smaller. The simulated and the measured values of the scattering parameters and the phase difference between S_{21} and S_{41} are shown in Fig. 21(b)–(d). The measured results of the scattering parameters at 2 GHz are $|S_{21}| = -3.65$ dB, $|S_{41}| = -3.8$ dB, $|S_{11}| = -15.44$ dB, and $|S_{31}| = -15.23$ dB. The phase difference between S_{21} and S_{41} is 91.74°.

D. Application to a Proof-of-Concept Marchand Balun

As a proof-of-concept demonstration for the capability of the proposed equivalent circuits to realize complicated structures using the directional couplers with arbitrary coupling coefficients and terminating impedances, an impedance-transforming (100 into 50 Ω) Marchand balun was designed at 2 GHz and fabricated. When $R_r = 100\ \Omega$, $R_L = 50\ \Omega$, and $C_0 = -6$ dB in (20), $Z_{0eR} = 100.48\ \Omega$ and $Z_{0oR} = 33.39\ \Omega$ are computed. Assuming a connecting segment of 30°, the values of $\Theta_{Ta1} = \Theta_{Ta2} = 15°$ were chosen, thus leading to $Z_{0ea1} = Z_{0ea2} = 102.91\ \Omega$, $Z_{0oa1} = Z_{0oa2} = 32.60\ \Omega$, and $\Theta_{a1} = \Theta_{a2} = 72.6°$ using (9), resulting the value of $Z_T = 57.92\ \Omega$. The isolation circuit is dependent on the termination impedances of R_L and if the isolation resistance
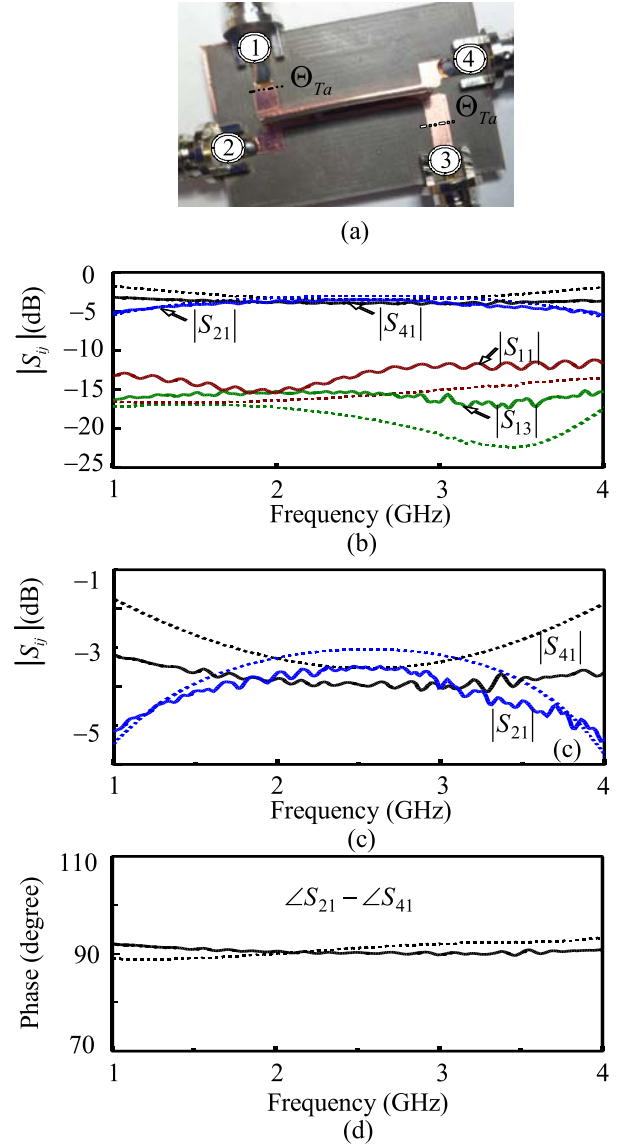

(a)

(b)

(c)

(d)

Fig. 21. Asymmetric equivalent circuit prototype along with a comparison of measured (solid lines) and predicted results (dotted lines). (a) Fabricated circuit. (b) Scattering parameters from port ①. (c) $|S_{21}|$ and $|S_{41}|$. (d) Phase difference between S_{21} and S_{41}.

of R_i is chosen to be the available resistance of 86.6 Ω, the characteristic impedance of Z_i is computed as 93.06 Ω, referring to [5, eq. (11)]. The design and fabrication data are presented collectively in Table VIII where the first line of the design data is related with the coupled transmission-line sections, the second one is about the transmission-line sections with Z_T, Θ_{Ta1}, and Θ_{Ta2}, and the third line presents the features of the isolation circuit. In a similar way, the first, second, and third rows of the fabrication data are those of the coupled transmission-line sections, uncoupled transmission-line sections, and the isolation circuit, respectively, following the asymmetric equivalent circuit configuration introduced in this paper.

The fabricated circuit is shown in Fig. 22(a) and the results measured and predicted are compared in Fig. 22(b) and (c) where the scattering parameters of matching at port ①, $|S_{11}|$, the power division of $|S_{21}|$ and the output matching at port
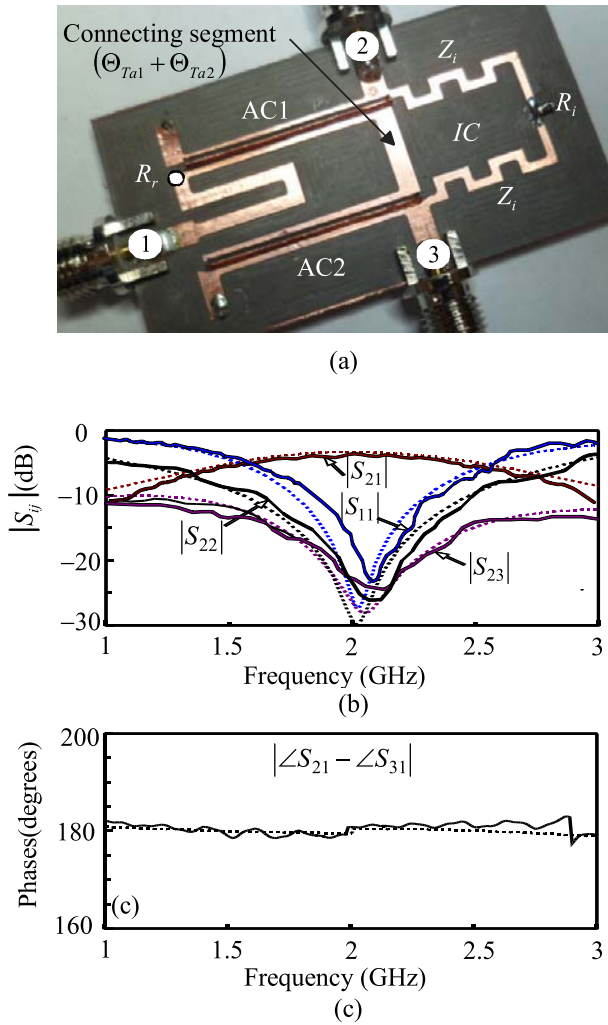
(a)

(b)

(c)

Fig. 22. Marchand balun topology along with the measured (solid lines) and predicted results (dotted lines). (a) Fabricated circuit. (b) Scattering parameters of $|S_{11}|$, $|S_{21}|$, $|S_{22}|$, and $|S_{23}|$. (c) Phase difference between S_{21} and S_{31}.

TABLE VIII
DESIGN AND FABRICATION DATA FOR THE PROOF-OF-CONCEPT
MARCHAND BALUN

Design data $R_r = 100\,\Omega$ $R_L = 50\,\Omega$	$Z_{0ea1} = Z_{0ea2} = 102.91\,\Omega$, $Z_{0oa1} = Z_{0oa2} = 32.6\,\Omega$, $\Theta_{a1} = \Theta_{a2} = 72.6^\circ$.
	$Z_T = 57.92\,\Omega$, $\Theta_{Ta1} = \Theta_{Ta2} = 15^\circ$.
	$Z_i = 93.06\,\Omega$, $\Theta_i = 90^\circ$, $R_i = 86.6\,\Omega$
Fabrication dimensions (mm)	$w_c = 0.9$, $g = 0.51$, $L_c = 22.35$
	$w_t = 1.87$, $L_t = 4.54$
	$w_i = 0.77$, $L_i = 27.90$

②, $|S_{22}|$ and the isolation of $|S_{23}|$ are in Fig. 22(b), while the phase difference between S_{21} and S_{31} in Fig. 22(c). The measured data at 2 GHz are $|S_{11}| = -15.78$ dB, $|S_{21}| = -3.45$ dB, $|S_{22}| = -24.60$ dB, and $|S_{23}| = -23.25$ dB. The phase difference between S_{21} and S_{31} in Fig. 22(c) is 182.78° at 2 GHz.

V. CONCLUSION

In this paper, three different equivalent circuits (asymmetric, symmetric, and mixed) for the 90° coupled transmission-line sections were suggested for the easy implementation of Marchand baluns, including the effect of the connecting segments of arbitrary lengths. The asymmetric topology consists of a set of coupled transmission-line sections and two identical uncoupled transmission-line sections. The symmetric one could be obtained using the even- and odd-mode equivalent circuits and the mixed one can be realized by combining the asymmetric and the symmetric ones. The frequency responses of the equivalent circuits were dependent on the electrical lengths of the uncoupled transmission-line sections and become more broadband for larger lengths of the uncoupled transmission-line sections.

Choosing one of the three novel generic equivalent circuit implementations based on fabrication and substrate constraints, the realization of Marchand baluns can be significantly simplified compared with other previously reported approaches.

REFERENCES

[1] N. Marchand, "Transmission line conversion transformers," *Electronics*, vol. 17, no. 12, pp. 142–145, Dec. 1944.
[2] K.-C. Lin and Y.-C. Lin, "A simple printed compensated balun for enhanced ultra-wideband performances," *IEEE Microw. Wireless Compon. Lett.*, vol. 24, no. 1, pp. 5–7, Jan. 2014.
[3] T. Canning, J. R. Powell, and S. C. Cripps, "Optimal design of broadband microwave baluns using single-layer planar circuit technology," *IEEE Trans. Microw. Theory Techn.*, vol. 62, no. 5, pp. 1183–1191, May 2014.
[4] H.-R. Ahn and T. Itoh, "New isolation circuits of compact impedance-transforming 3-dB baluns for theoretically perfect isolation and matching," *IEEE Trans. Microw. Theory Techn.*, vol. 58, no. 12, pp. 3892–3902, Dec. 2010.
[5] H.-R. Ahn and S. Nam, "New design formulas for impedance-transforming 3-dB Marchand baluns," *IEEE Trans. Microw. Theory Techn.*, vol. 59, no. 11, pp. 2816–2823, Nov. 2011.
[6] K. Nishikawa, I. Toyoda, and T. Tokumitsu, "Compact and broad-band three-dimensional MMIC balun," *IEEE Trans. Microw. Theory Techn.*, vol. 47, no. 1, pp. 96–98, Jan. 1999.
[7] T.-G. Ma and Y.-T. Cheng, "A miniaturized multilayered Marchand balun using coupled artificial transmission lines," *IEEE Microw. Wireless Compon. Lett.*, vol. 19, no. 7, pp. 446–448, Jul. 2009.
[8] T.-G. Ma, C.-C. Wang, and C.-H. Lai, "Miniaturized distributed Marchand balun using coupled synthesized CPWs," *IEEE Microw. Wireless Compon. Lett.*, vol. 21, no. 4, pp. 188–190, Apr. 2011.
[9] C.-H. Lin, C.-H. Wu, G.-T. Zhou, and T.-G. Ma, "General compensation method for a Marchand balun with an arbitrary connecting segment between the balance ports," *IEEE Trans. Microw. Theory Techn.*, vol. 61, no. 8, pp. 2821–2830, Aug. 2013.
[10] G. Yang, Z. Wang, Z. Li, Q. Li, and F. Liu, "Balance-compensated asymmetric Marchand baluns on silicon for MMICs," *IEEE Microw. Wireless Compon. Lett.*, vol. 24, no. 6, pp. 391–393, Jun. 2014.
[11] I. Piekarz, J. Sorocki, S. Gruszczynski, and K. Wincza, "Input match and output balance improvement of Marchand balun with connecting line," *IEEE Microw. Wireless Compon. Lett.*, vol. 24, no. 10, pp. 683–685, Oct. 2014.
[12] H. R. Ahn and B. Kim, "Transmission-line directional couplers for impedance transforming," *IEEE Microw. Wireless Compon. Lett.*, vol. 16, no. 10, pp. 537–539, Oct. 2006.
[13] G. I. Zysman and A. K. Johnson, "Coupled transmission line networks in an inhomogeneous dielectric medium," *IEEE Trans. Microw. Theory Techn.*, vol. 17, no. 10, pp. 753–759, Oct. 1969.
[14] H.-R. Ahn, *Asymmetric Passive Components in Microwave Integrated Circuits*. New York, NY, USA: Wiley, 2006.

Hee-Ran Ahn (S'90–M'95–SM'99) received the B.S., M.S., and Ph.D. degrees from Sogang University, Seoul, South Korea, all in electronic engineering.

From 1996 to 2002, she was with the Department of Electrical Engineering, Duisburg–Essen University, Duisburg, Germany, where she was involved with the Habilitation dealing with asymmetric passive components in microwave circuits. From 2003 to 2005, she was with the Department of Electrical Engineering and Computer Science, Korea Advanced Institute of Science and Technology (KAIST), Daejeon, South Korea. From 2005 to 2009, she was with the Department of Electronics and Electrical Engineering, Pohang University of Science and Technology, Pohang, South Korea. From 2009 to 2010, she was with the Department of Electrical Engineering, University of California Los Angeles, Los Angeles, CA, USA. From 2011 to 2014, she was with the School of Electrical Engineering and Computer Science, Seoul National University, Seoul, South Korea. Since 2015, she has been with the School of Electrical and Computer Engineering, Georgia Institute of Technology, Atlanta, GA, USA, as a Visiting Scholar. She authored *Asymmetric passive component in microwave integrated circuits* (Wiley, 2006). Her current research interests include high-frequency and microwave circuit designs and biomedical applications using microwave theory and techniques.

Manos M. Tentzeris (S'94–M'98–SM'03–F'10) received the Diploma degree (*magna cum laude*) in electrical and computer engineering from the National Technical University of Athens, Athens, Greece, and the M.S. and Ph.D. degrees in electrical engineering and computer science from the University of Michigan, Ann Arbor, MI, USA.

He has served as the Head of the GT-ECE Electromagnetics Technical Interest Group, an Associate Director with the Georgia Electronic Design Center for RFID/sensors research, and an Associate Director with the NSF-Packaging Research Center, Georgia Institute of Technology, Atlanta, GA, USA, for RF Research and the RF Alliance Leader. He is currently a Ken Byers Professor of flexible electronics with the School of Electrical and Computer Engineering, Georgia Institute of Technology. He was a Visiting Professor with the Technical University of Munich, Germany, in 2002, a Visiting Professor with GTRI-Ireland, Athlone, Ireland, in 2009, and a Visiting Professor with LAAS-CNRS, Toulouse, France, in 2010. He has given over 100 invited talks to various universities and companies all over the world. He has authored over 620 papers in refereed journals and conference proceedings, 5 books, and 25 book chapters. He has helped develop academic programs in 3-D/inkjet-printed RF electronics and modules, flexible electronics, origami and morphing electromagnetics, highly integrated/multilayer packaging for RF and wireless applications using ceramic and organic flexible materials, paper-based RFID's and sensors, wireless sensors and biosensors, wearable electronics, Green electronics, energy harvesting and wireless power transfer, nanotechnology applications in RF, microwave MEM's, SOP-integrated (UWB, multiband, mmW, and conformal) antennas and heads the ATHENA research group (20 researchers).

Dr. Tentzeris is a member of the URSI-Commission D, a member of the MTT-15 Committee, an Associate Member of EuMA, a Fellow of the Electromagnetic Academy, and a member of the Technical Chamber of Greece. He served as one of the IEEE MTT-S Distinguished Microwave Lecturers from 2010 to 2012 and the IEEE CRFID Distinguished Lecturers. He was a recipient/co-recipient of the 2015 IET Microwaves, Antennas and Propagation Premium Award, the 2014 Georgia Institute of Technology ECE Distinguished Faculty Achievement Award, the 2014 IEEE RFID-TA Best Student Paper Award, the 2013 IET Microwaves, Antennas and Propagation Premium Award, the 2012 FiDiPro Award in Finland, the iCMG Architecture Award of Excellence, the 2010 IEEE Antennas and Propagation Society Piergiorgio L. E. Uslenghi Letters Prize Paper Award, the 2011 International Workshop on Structural Health Monitoring Best Student Paper Award, the 2010 Georgia Institute of Technology Senior Faculty Outstanding Undergraduate Research Mentor Award, the 2009 IEEE TRANSACTIONS ON COMPONENTS AND PACKAGING TECHNOLOGIES Best Paper Award, the 2009 E. T. S. Walton Award from the Irish Science Foundation, the 2007 IEEE AP-S Symposium Best Student Paper Award, the 2007 IEEE MTT-S IMS Third Best Student Paper Award, the 2007 ISAP 2007 Poster Presentation Award, the 2006 IEEE MTT-S Outstanding Young Engineer Award, the 2006 Asian–Pacific Microwave Conference Award, the 2004 IEEE TRANSACTIONS ON ADVANCED PACKAGING Commendable Paper Award, the 2003 NASA Godfrey Art Anzic Collaborative Distinguished Publication Award, the 2003 IBC International Educator of the Year Award, the 2003 IEEE CPMT Outstanding Young Engineer Award, the 2002 International Conference on Microwave and Millimeter-Wave Technology Best Paper Award in Beijing, China, the 2002 Georgia Institute of Technology ECE Outstanding Junior Faculty Award, the 2001 ACES Conference Best Paper Award and the 2000 NSF CAREER Award, and the 1997 Best Paper Award of the International Hybrid Microelectronics and Packaging Society. He was the TPC Chair of the IEEE IMS 2008 Symposium and the Chair of the 2005 IEEE CEM-TD Workshop. He is the Vice-Chair of the RF Technical Committee (TC16) of the IEEE CPMT Society. He is the Founder and the Chair of the RFID Technical Committee (TC24) of the IEEE MTT-S and the Secretary/Treasurer of the IEEE C-RFID. He is an Associate Editor of the IEEE TRANSACTIONS ON MICROWAVE THEORY AND TECHNIQUES, the IEEE TRANSACTIONS ON ADVANCED PACKAGING, and the *International Journal on Antennas and Propagation*.